OE Optical Engineering

RESEARCH PAPER

Imaging and detection method for low signal-to-noise ratio airborne synthetic aperture ladar signals

Jinghan Gao,[a,b] Daojing Li,[a,*] Kai Zhou,[a,b] Anjing Cui,[a,b] Jiang Wu,[a,b] Shumei Wu,[a] Yefei Wang,[c] Kai Liu,[c] Songnian Tan,[c] Yang Gao,[c] and Yuan Yao[c]

[a]Chinese Academy of Sciences, Aerospace Information Research Institute, National Key Laboratory of Microwave Imaging Technology, Beijing, China

[b]University of Chinese Academy of Sciences, School of Electronics, Electrical, and Communication Engineering, Beijing, China

[c]Chinese Academy of Sciences, Changchun Institute of Optics, Fine Mechanics, and Physics, Changchun, China

ABSTRACT. Vibration greatly impairs the imaging quality of airborne synthetic aperture ladar (SAL), so the vibration phase error must be estimated and compensated before imaging. Limited by the laser's average power, the high pulse repetition frequency of the SAL will result in lower peak-power of the laser, thereby reducing the echo signal's single-pulse signal-to-noise ratio (SNR). In the case of a low SNR, the coherence between channels worsens, and the vibration phase-error compensation method based on interferometry is difficult to apply. We analyze the imaging SNR and resolution of the echo signal when the airborne SAL observes noncooperative targets by intentionally broadening the transmitting and receiving beams, discussing the imaging processing flow of the low SNR signal under conditions of beam-broaden and platform vibration. The data processing flow includes the phase correction of the echo signal using the transmitting reference channel signal. Based on the flight parameters of the airborne SAL, the echo was dechirped and narrowband filtered to reduce noise. After subaperture division, the spatial correlation algorithm was used to estimate and compensate the vibration phase error, and the range-Doppler algorithm was used to achieve strip imaging. At the same time, the phase gradient autofocus algorithm was introduced to improve the focusing effect. The processing results of flight experiment data of the airborne SAL corresponding to noncooperative targets at 1 km demonstrated the effectiveness of the proposed method.

Keywords: synthetic aperture ladar; ladar; airborne imaging systems; low signal-to-noise ratio; vibration phase-error compensation

Paper 20230193G received Mar. 1, 2023; revised Sep. 12, 2023; accepted Sep. 19, 2023; published Sep. 27, 2023.

1 Introduction

Ladar imaging systems, such as traditional optical imaging systems, have spatial resolution limited by the optical aperture of the system, and the resolution decreases with the increase of distance. Therefore, high-resolution long-distance imaging systems often require a large optical aperture. However, in existing systems, many factors limit the increase in the optical aperture of the system. Synthetic aperture ladar (SAL) can effectively address this problem. SAL uses the

*Address all correspondence to Daojing Li, lidj@mail.ie.ac.cn

0091-3286/2023/$28.00 © 2023 SPIE

principle of synthetic aperture to form a synthetic aperture that is much larger than the actual aperture. Its resolution does not decrease with the increased distance and it can obtain high-resolution images quickly. These characteristics allow ladar to realize long-distance high-resolution imaging and offer great application potential and broad prospects for development in military reconnaissance and remote sensing mapping.

Airborne SAL is limited by the laser power density on the target and the number of receiving channels, and its transmitting and receiving beam width is generally narrow, which makes it difficult for airborne SAL to obtain a large observation width. The imaging targets in the airborne SAL flight experiments publicly reported have primarily been high-reflectivity cooperative targets,[1–3] and the observation width has been narrow. For example, in 2011, Lockheed Martin independently conducted flight experiments on an airborne SAL system. For high-reflectivity cooperative targets at a distance of 1.6 km, they achieved an imaging result of 1 m width at a resolution better than 3.3 cm. In the imaging process, they used the phase gradient autofocus (PGA)[4,5] algorithm of microwave synthetic aperture radar to suppress the impact of vibration.

In order to form a larger observation width, it is usually necessary to broaden the transmitting and receiving beams. The commonly used beam-broaden methods include using a beam expander lens to broaden the transmitting beam and an array detector to broaden the receiving beam equivalently. Taking an optical system with a diameter of 100 mm and a focal length of 480 mm as an example, it is assumed that a unit detector with a photosensitive surface size of 9.5 μm is used for reception. When the central wavelength is 1.55 μm, the corresponding receiving beam width is about 20 μrad, close to the diffraction limit. The detector array size required to cover the receiving field of view (FOV) of 3 mrad is 150×150, which will lead to a considerable amount of data and make the technical implementation of the system extremely complex.

To expand the observation width and simplify the system, the elevation direction beam of the airborne SAL can be broadened, and a few detectors can be used to receive the wide FOV laser signal. However, the beam-broadening will also significantly reduce the echo signal's imaging signal-to-noise ratio (SNR). Since the imaging SNR of SAL can be improved by signal processing after analog-to-digital converter (ADC) sampling, the use of electronic amplifiers combined with signal processing methods can compensate to a certain extent for the loss caused by the broadening of the transmitting and receiving beams.[6]

In addition, the vibration of airborne SAL platforms can significantly reduce the imaging resolution and SNR. Limited by the laser's average power, the high pulse repetition frequency (PRF) of the SAL will result in lower peak-power of the laser, thereby reducing the echo signal's single-pulse SNR. In the case of a low SNR, the coherence between channels becomes worse, and the vibration phase-error compensation method based on interferometry is difficult to apply.[7–10] Therefore, it is important to study the SAL signal processing methods of airborne SAL low SNR signals under vibration and beam-broadening conditions.

In this paper, transmitting and receiving beam-broaden technology is used to set the width of a single channel of the SAL system in the range direction to 6.3 m (the largest publicly reported single-channel width of an airborne SAL). The scanning of the photoelectric ball is combined to further expand the observation width. On this basis, to address the low SNR problem caused by target characteristics, beam-broadening, and vibration, this paper proposes a data processing method to solve the imaging and vibration phase-error compensation of airborne SAL in the case of low SNR. In addition, we introduced our developed beam expansion airborne SAL system and conducted flight experiments on noncooperative targets for the first time. The effectiveness of the proposed data processing method was verified through simulation and experimental results.

2 SAL System Introduction and Performance Analysis

2.1 System Introduction

The SAL prototype system block diagram is shown in Fig. 1. The fiber laser generates and transmits a high-power narrow-pulse laser signal. The laser signal is reflected by the target, received by the balance detector, amplified by the electronic low noise amplifier, and then sampled by ADC. In addition, as the laser signal is transmitted, the time-variant phase of the transmitting signal is also sampled by the transmitting reference channel in a spatially coupled manner

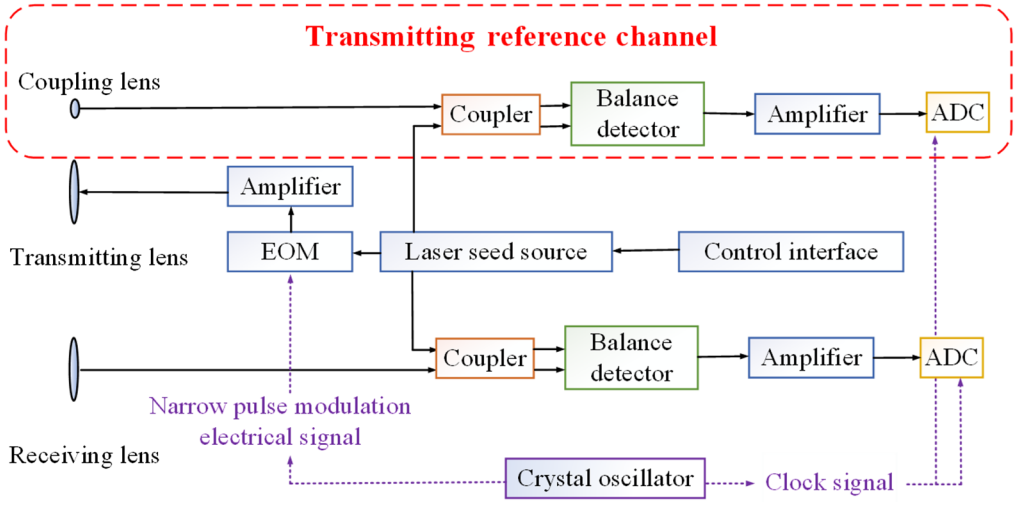

Fig. 1 SAL system block diagram.

(coupling a tiny portion of the emitted signal into the optical fiber through a lens) for subsequent nonlinear phase correction. To ensure the system's coherence, we use the same crystal oscillator to generate the narrow pulse modulation electrical signal of the electro-optic modulator and the clock signal of the ADC.

The structure of the SAL system in this paper is a photoelectric ball. The laser transceiver system adopts an all-fiber optical path, and an aviation stabilization platform is used to suppress its vibration. This installation method can ensure that the system works normally under the two-dimensional rotation of the photoelectric ball. During the flight experiment, the position and orientation system (POS) is used to obtain the position and speed information of SAL, and the beam pointing information of SAL can be calculated by combining the encoding disk data of the photoelectric ball.

2.2 Flight Experiment Parameters

The schematic diagram of the SAL system photo, transmitting and receiving beams, and flight experimental observation geometry in this paper is shown in Fig. 2. The transmitting and receiving beams are broadened in the elevation direction to expand the instantaneous observation width in the range direction and combined with the elevation direction scanning of the photoelectric ball. The range observation width of the system is further expanded. The width of the transmitting beam is 5 mrad(elevation direction) × 100 μrad(azimuth direction), and the width of the receiving beam is 3 mrad(elevation direction) × 3 mrad(azimuth direction). Four partially overlapping receiving beams cover the width of the transmitting beam in the elevation direction of 5 mrad. This paper discusses the processing of the echo signal of one receiving channel.

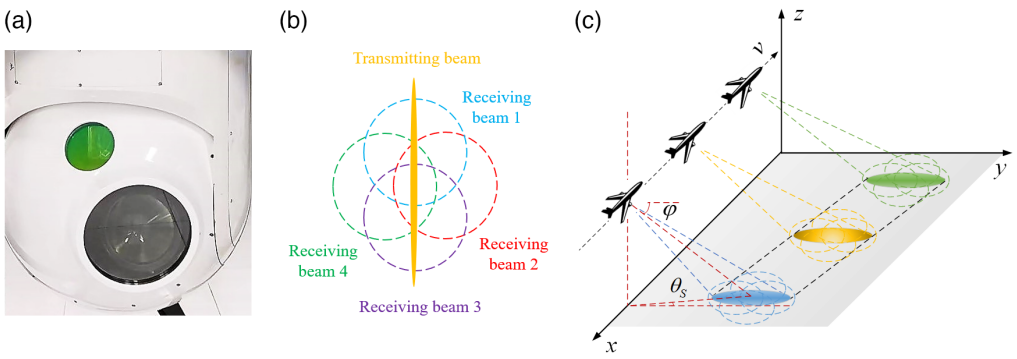

Fig. 2 Schematic diagram of the SAL system: (a) photo of the photoelectric ball, (b) transmitting and receiving beams, and (c) flight experimental observation geometry.

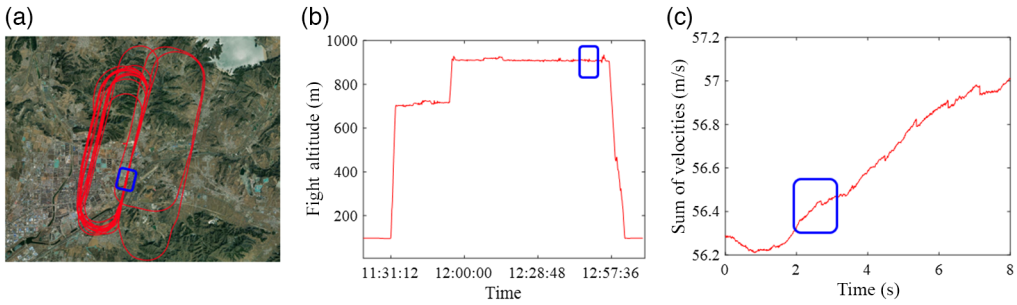

Fig. 3 Schematic of the flight parameters: (a) flight path, (b) platform altitude, and (c) flight velocity.

Based on the above observation geometry, the flight experiment of the SAL system was carried out. The corresponding flight path, platform altitude, and flight velocity data are shown in Fig. 3. The period corresponding to the data used in this paper is marked with the blue line box. During this period, the average altitude of the platform was 919 m, the altitude of the experimental area was 97 m, and the corresponding average flight height was 812 m. In addition, the average flight velocity $V = 56.4$ m/s. According to the POS data and the encoding disk data of the photoelectric ball, the squint angle $\theta_s = -0.3$ deg and the depression angle $\varphi = 53.1$ deg were calculated.

2.3 System Parameters

The SNR of the SAL echo signal can be characterized as follows:

$$R_{\mathrm{SN}} = \frac{\eta_d \cdot \eta_{\mathrm{wid}} \cdot \xi \cdot \eta_{\mathrm{sys}} \cdot \eta_{\mathrm{ato}} \cdot P_t \cdot G_t \cdot \rho \cdot A_t \cdot A_r}{4\pi \cdot \Omega \cdot R^4 \cdot F_n \cdot h \cdot f_c \cdot B}, \tag{1}$$

where R_{SN} is the SNR of the echo signal, P_t is the peak-power of the transmitted signal, $A_r = \pi D^2/4$ is the effective receiving area of the receiving telescope, D is the diameter of the receiving telescope, $G_t = 4\pi/(\theta_a\theta_e)$ is the transmission gain, θ_e is the width of the transmitting beam in the elevation direction, θ_a is the width of the transmitting beam in the azimuth direction, $\eta_{\mathrm{wid}} = (\lambda/D)^2/(\varphi_a\varphi_e)$ is the receiving beam-broadening loss factor, λ is the wavelength of the laser signal, φ_e is the width of the receiving beam in the elevation direction, φ_a is the width of the receiving beam in the azimuth direction, R is the distance between the ladar and the target, ρ is the average reflection coefficient of the target, A_t is the target area, Ω is the target scattering solid angle, η_{ato} is the two-way atmospheric loss factor, η_{sys} is the system loss factor, including the electronic loss and optical loss, f_c is the frequency of the laser signal, h is Planck's constant, F_n is the electronic noise figure, T_p is the pulse width, ξ is the polarization loss factor, η_d is the photoelectric conversion efficiency of the detector, and $B = 1/T_p$ is the signal bandwidth.

The parameters of the SAL system in this paper are shown in Table 1. The beamwidth corresponding to one receiving channel is used to analyze the SNR of the echo signal. If the target range of the SAL is 1 km, the single-sample SNR calculated is −6.28 dB.

Considering the gain of signal processing on the SNR of the echo signal, the SNR after the pulse compression processing in the range direction and the synthetic aperture processing in the azimuth direction is as follows:

$$R_{\mathrm{SN}} = \frac{\eta_d \cdot \eta_{\mathrm{wid}} \cdot \xi \cdot \eta_{\mathrm{sys}} \cdot P_{\mathrm{t}} \cdot G_t \cdot \rho \cdot A_t \cdot A_r}{4\pi \cdot \Omega \cdot R^4 \cdot F_n \cdot h \cdot f_c \cdot B} \cdot (T_p \cdot B_s) \cdot (T_{\mathrm{sa}} \cdot B_d), \tag{2}$$

where $T_{\mathrm{sa}} \cdot B_d$ is the gain of synthetic aperture processing (the number of coherently accumulated pulses), T_{sa} is the synthetic aperture time, B_d is the Doppler bandwidth (PRF), $T_p \cdot B_s$ is the gain of pulse compression processing, and B_s is signal bandwidth. In this paper, the SAL system uses the narrow Gaussian pulse of 5 ns, corresponding to $T_p \cdot B_s \approx 1$.

Table 1 SAL system parameters.

Parameter	Value	Parameter	Value
P_T	20 kW	Average power	10 W
T_p	5 ns	PRF	100 kHz
θ_e	5 mrad	θ_a	100 μrad
φ_e	3 mrad	φ_a	3 mrad
λ	1.55 μm	D	100 mm
η_d	0.5	η_{ato}	0.8
η_{sys}	0.4	F_n	3 dB
A_t	0.0075 m^2	η_{wid}	−44.5 dB
Ω	0.1 sr	ρ	0.3
ξ	0.4	B	200 MHz

The maximum synthetic aperture time T_{sa} can be expressed by the following formula:

$$T_{sa} = \frac{R\theta_a}{V \cos\theta_s \cos\varphi}. \tag{3}$$

The synthetic aperture time corresponds to the slow-time pulse number. Considering the slow-time Fourier transform, the pulse number is usually rounded down to an integer power of 2. Combined with the parameters of the flight experiment, the synthetic aperture time is ~2.56 ms, and the corresponding number of pulses that can be coherently accumulated is 256. In the case of fully compensating for the phase error, the SNR can be improved by 24.08 dB, and the corresponding imaging SNR is 17.8 dB. The target corresponding to this SNR has an average reflection coefficient of 0.3 and a scattering solid angle of 0.1 sr, which is a target with high reflectivity. Considering the complexity of ground objects, the influence of platform vibration, and the incompleteness of phase-error compensation, the imaging SNR of most ground objects will be lower than this value.

3 Processing Flow and Imaging Simulation

3.1 Processing Flow

For low SNR imaging requirements under vibration and beam-broaden conditions, the data processing flow is as shown in Fig. 4. Because nonorthogonal single-channel ADC sampling is adopted, the sampled signals are real signals, which need to be transformed by fast-time Hilbert transform to form the complex signal required for subsequent imaging, and then the direct-current component and clutter interference are filtered in the fast-frequency domain and slow-frequency domain, respectively.

The matched filter is constructed with the transmitted reference signal and matched with the echo signal in the fast-frequency domain to realize the correction of nonlinear phase in the echo signal.[11,12] Since the single-pulse SNR of the echo signal after correction is still low, the time–frequency analysis method can be used for data browsing, and the signal duration and time segment can be estimated from the time–frequency analysis results.

The observed geometric parameters of the airborne SAL are estimated from the POS data and the encoding disk data of the photoelectric ball. The Doppler modulation frequency rate (Ka) is then calculated according to the observed geometric parameters, and the matched filter required by the range-Doppler (RD) algorithm is constructed at the zero frequency of the Doppler frequency. The filter bandwidth can be calculated with the following formula:

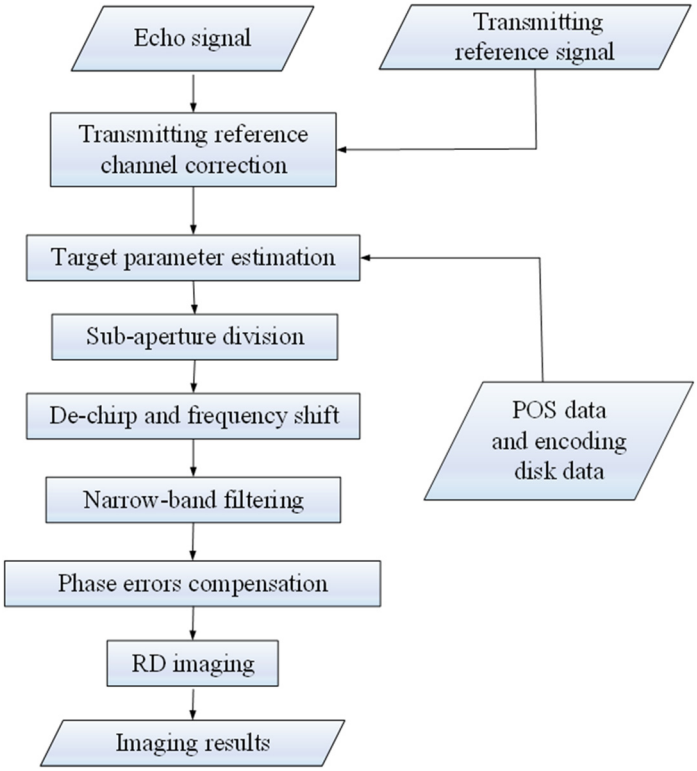

Fig. 4 Data processing flowchart.

$$B_a = \frac{2V}{\lambda}\theta_a \cos\theta_s \cos\varphi = 4.37 \text{ kHz}. \tag{4}$$

The Doppler frequency rate (K_a) can be expressed as follows:

$$K_a = \frac{B_a}{T} = \frac{2V^2 \cos^2\theta_s \cos^2\varphi}{\lambda R} = 1.46 \text{ MHz/s}. \tag{5}$$

Considering that the target scene is mostly discontinuous and the elevation scanning of the photoelectric sphere will cause the instantaneous variation of the Doppler center frequency of the target, it is necessary to divide the echo signal into subapertures and estimate the Doppler center frequency of the target and then perform dechirp and frequency-shift processing for the signal of each subaperture. The signal after dechirp and frequency shift is concentrated in the low-frequency region. At this time, narrowband filtering can be done in the Doppler frequency domain to improve the time-domain SNR, creating conditions for using spatial correlation algorithm (SCA).[13]

After narrow-band filtering, SCA based on pulse-train correlation is used to reduce the impact of noise and implement vibration phase-error compensation for the signal of each subaperture. The compensated signal is then imaged with the RD algorithm, and the imaging results of each subapertures are spliced to obtain a long-term image. To improve the focusing effect of the image in the azimuth direction, the PGA algorithm can be used to process the echo signal based on compensating for the vibration phase error using the SCA. In this process, the SCA plays an essential role in imaging. If the echo signal cannot be focused after SCA processing, there is deemed to be no echo signal within this period.

3.2 Imaging Simulation

For airborne SAL, due to the short wavelength of the laser, the μm-level vibration of the airborne platform can cause significant variations in the signal's phase, which can significantly affect the imaging results. Consequently, it is necessary to compensate for the vibration phase error before performing imaging processing.

Currently, the methods for estimating the vibration phase error of SAL signals include the SCA and the PGA algorithm. The SCA is proposed for airborne SAL. Its primary function is to extract the differential value of the vibration phase error from the complex correlation coefficient of adjacent echo pulses and accumulate the differential value backward to estimate it. The key to estimate the vibration phase error of the airborne SAL signal is the strong correlation between the echo signals corresponding to adjacent pulses. This strong correlation is due to the higher PRF of the airborne SAL and the relatively uniform backscattering characteristics of the target in the laser band. Since the scattering characteristics of the target scene corresponding to the laser band always vary slowly, in this paper—where the size in the azimuth direction of the transmitted laser spot is as small as 0.1 m—it can be considered that the scattering characteristics of the target in the ground laser spot are uniformly distributed along the azimuth direction. Moreover, the PRF of the airborne SAL system in this paper is 100 kHz, and the offset of the ground spot corresponding to adjacent pulses in the azimuth direction is about 1 mm, providing conditions for the use of the SCA to estimate the vibration phase error.

3.2.1 *Subaperture division*

Due to its short laser wavelength, SAL can obtain sufficient bandwidth within a short synthetic aperture time to meet high-resolution imaging requirements, making it possible for SAL to divide subapertures in the slow-time domain and perform subaperture imaging. Because the stabilization platform limits the amplitude and frequency of vibration, they change very little in subaperture time. Consequently, the imaging time can be reduced by dividing the subaperture to limit the impact of vibration on the signal. Additionally, for noncooperative targets, the scattering points that meet the SNR requirements in the target scene are mostly isolated single scattering points, with the discontinuity of each scattering point causing the SCA to fail to accurately estimate the vibration phase error. Since the signal characteristics are not obvious in the case of a low SNR, it can be difficult to accurately judge the duration of each scattering point. However, the signal can be divided into subapertures in the slow-time domain in the form of a sliding window, and the vibration phase error is estimated using the SCA.

The synthetic aperture time is ~2.56 and 5.12 ms is a subaperture time, each overlapping by 2.56 ms in slow time. The 2.56 ms at the center of each subaperture can be used for splicing the imaging results. A schematic of the subaperture division process is shown in Fig. 5.

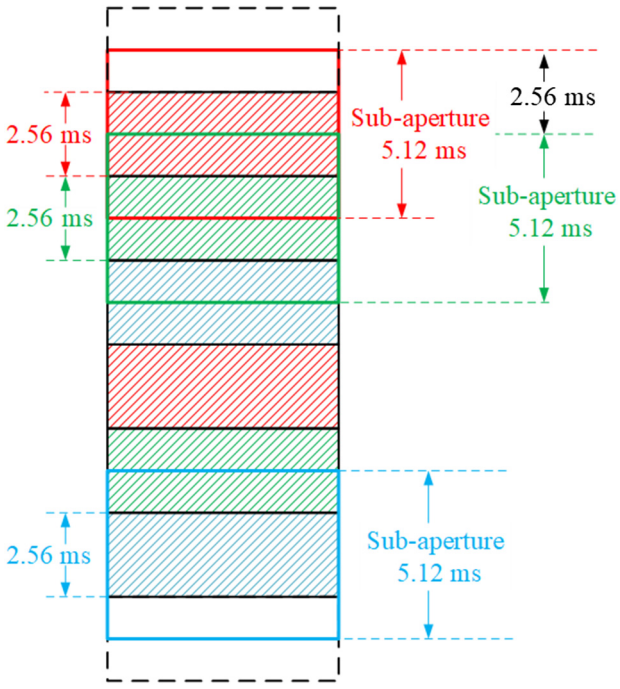

Fig. 5 Schematic of subaperture division.

3.2.2 *Dechirp and narrow-band filtering*

In the case of a low SNR, the noise phase constitutes the main component. Consequently, when extracting the differential value of the vibration phase error, the noise can cause error and potentially lead to the failure of phase unwrapping, thereby reducing the estimation accuracy of the vibration phase error of the SCA. Since the PRF of the SAL is usually much higher than the vibration frequency, the vibration phase error varies at a constant velocity in the period corresponding to several pulses. In this case, the method of using multiple pulses to calculate the complex correlation coefficient can be used, which is equivalent to statistically averaging the noise interferometry, reducing the impact of noise on the SCA estimation accuracy.

Additionally, since the signal after dechirping only occupies a small part of the entire Doppler frequency domain, the influence of the noise phase on the SCA estimation accuracy can be further reduced by conducting narrow-band filtering before using the SCA. In the simulations, the SNR was set to −6 dB; the other parameters are shown in Table 1. A comparison between the phase curves estimated using the SCA before and after narrow-band filtering and the phase curve of the real vibration value is shown in Fig. 6.

It is evident that after narrow-band filtering (with a bandwidth of 20 kHz), the estimation accuracy of the SCA increases considerably, and the estimated vibration phase-error curve is closer to the phase curve of the real vibration value. The residual phase error can be further estimated and compensated using the PGA algorithm.

3.2.3 *Phase-error compensation and imaging simulation*

Based on the parameters discussed in Sec. 2 and the data processing flow shown in Fig. 4, an imaging simulation of the SAL echo signal was performed; the simulated target scene is as shown in Fig. 7. The x axis is the cross-track direction, the y axis is the along-track direction, and the z axis is the vertical direction from the ground.

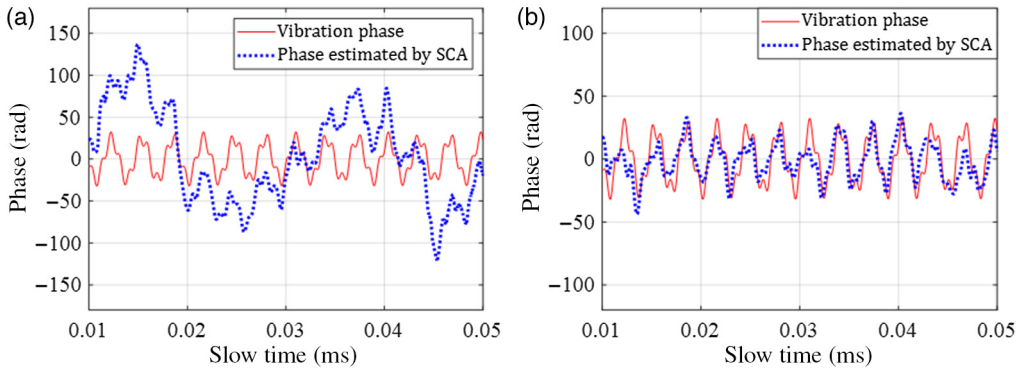

Fig. 6 Effect of narrow-band filtering on the estimation accuracy of the vibration phase error using the SCA: (a) before narrow-band filtering and (b) after narrow-band filtering.

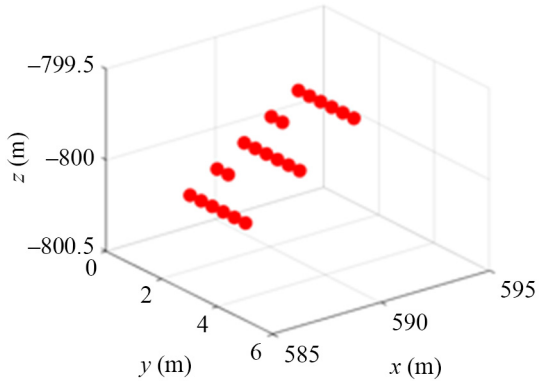

Fig. 7 Target scene of the simulation.

The flight altitude is 800 m, the depression angle is 60 deg, the average flight velocity is 56 m/s, and the squint angle is 0.2 deg. The target used for imaging is the character "*E*." The distance between the five points in the cross-track direction is 1.2 m, and the distance between the six points in the along-track direction is 0.4 m. The single-pulse SNR of the echo signal is −6 dB. The vibration frequencies are 300 and 1100 Hz, and the maximum vibration amplitude is 1 μm.

By dividing the subaperture and dechirping the received echo signal, we can estimate the Doppler center frequency, shift the signal to zero frequency, and perform narrow-band filtering to reduce noise interferometry. The time–frequency analysis results corresponding to the center range gate are shown in Fig. 8 (the time–frequency analysis window length is 2.56 ms, and the overlap length is 1.28 ms). The red dotted line in Fig. 8 marks the signal area to assist in analysis.

The size of the azimuth direction of the target is 2 m, and the corresponding echo signal duration is 35.7 ms. According to Fig. 5, 14 subapertures can be divided, and the time–frequency analysis results of each subaperture are shown in Fig. 9(a). When the spot size is larger than the target size, the phase estimated by the SCA not only includes the vibration phase error but also the second-order phase corresponding to the translational component of the platform. After compensating for the phase estimated using the SCA, the second-order phase corresponding to the translational component must also be compensated. After narrow-band filtering using a band-

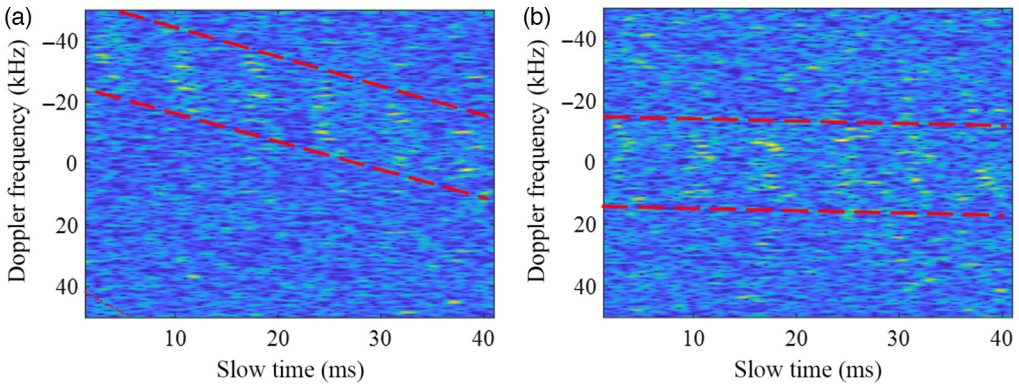

Fig. 8 Time–frequency analysis results: (a) original echo signal and (b) echo signal after dechirping and frequency shifting.

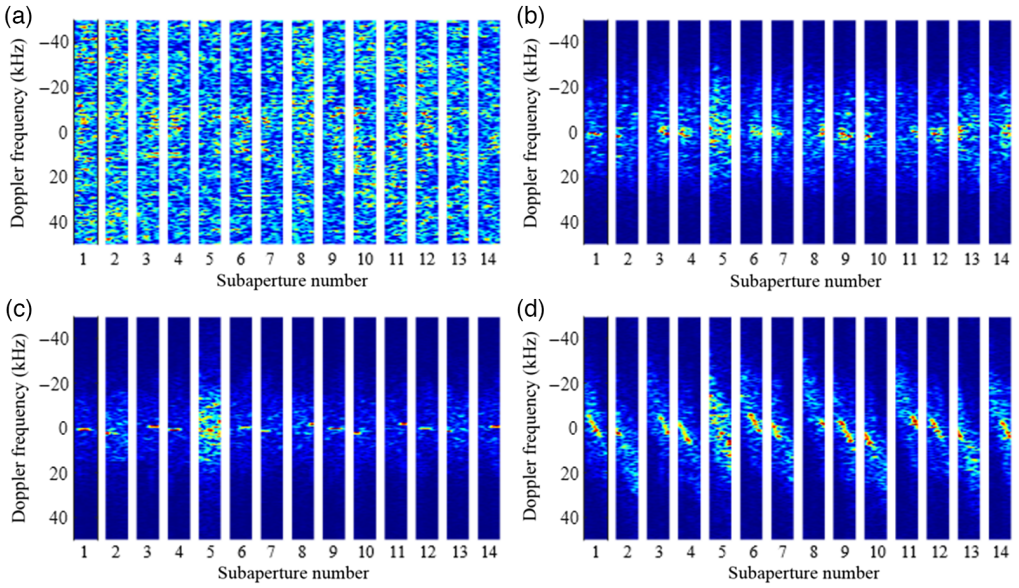

Fig. 9 Time–frequency analysis results of each subaperture: (a) before vibration phase-error compensation, (b) after SCA compensation, (c) after PGA processing, and (d) after compensating for the second-order phase.

pass filter bandwidth of 40 kHz, the phase error is estimated by the SCA (calculating the complex correlation coefficient with four pulses); the time–frequency analysis results of each subaperture after compensating for the phase error are shown in Fig. 9(b).

Evidently, after SCA compensation, the image has been preliminarily focused. The echo signal corresponding to the first scattering point is in the first and second subaperture, the echo signal corresponding to the second scattering point is in the third and fourth subaperture, the echo signal corresponding to the third scattering point is in the sixth and seventh subaperture, the echo signal corresponding to the fourth scattering point is in the eighth to tenth subaperture, the echo signal corresponding to the fifth scattering point is in the eleventh to thirteenth subaperture, and the echo signal corresponding to the sixth scattering point is in the fourteenth subaperture.

It should be noted that the reason the fifth subaperture is not focused after SCA compensation is that there is no echo signal in the fifth subaperture. It is evident from Fig. 9(b) that the SNR of the echo signal improves after SCA compensation, but defocusing still exists due to the influence of the residual phase error, which provides conditions for the use of the PGA algorithm. The result after PGA processing is shown in Fig. 9(c); it is evident that the signals of each subaperture are further focused. Consequently, the influence of the linear phase of the PGA process in each subaperture is removed, and the second-order phase corresponding to the translational component is compensated for, as shown in Fig. 9(d).

The Doppler frequency rate is estimated based on the velocity, the matched filter is constructed, and the data of each subaperture are input into the matched filter for imaging. The bandwidth of the matched filter is ∼6 kHz, and the corresponding azimuth resolution is 1.0 cm. The imaging results before vibration phase-error compensation, after SCA compensation, and after further focusing using the PGA algorithm are shown in Fig. 10—that is, Figs. 10(d)–10(f) shows the profile of Figs. 10(a)–10(c) in the azimuth direction. The imaging results before the vibration phase-error compensation are shown in Figs. 10(a) and 10(d). The distance in the azimuth direction of the imaging results is defined as the cross range, and the

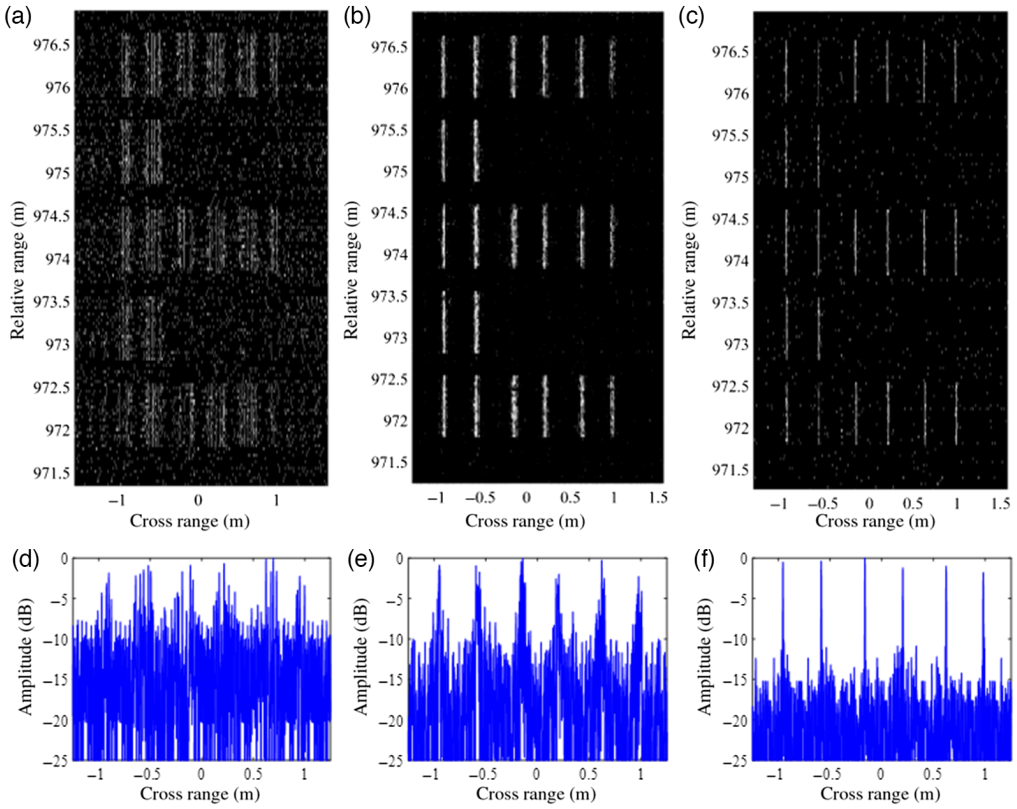

Fig. 10 Imaging results: (a), (d) before compensation; (b), (e) after SCA compensation of the vibration phase error; and (c), (f) after SCA compensation and then processed using the PGA algorithm.

Table 2 Image entropy, image contrast, and image SNR of imaging results.

	Fig. 10(a)	Fig. 10(b)	Fig. 10(c)
Entropy	13.4437	12.7420	11.9606
Contrast	0.6049	0.6999	0.8672
SNR (dB)	10	14	17

distance in the slant-range direction is defined as the relative range. It is evident that the imaging results are defocused, and the target outline is blurred. The imaging results after using the SCA to estimate and compensate for the vibration phase error are shown in Figs. 10(b) and 10(e). Clearly, after compensating for the vibration phase error using the SCA, the focus effect of the image improves, and the outline of the target becomes clearer, showing that the SCA can be used for the preliminary estimation of the SAL vibration phase error.

Figures 10(c) and 10(f) show the imaging results after compensating for the vibration phase error using the SCA and then compensating for the residual phase error using the PGA algorithm. Here the focus effect of the image further improves, and the azimuth resolution is close to the theoretical resolution of 1 cm.

The focusing effect of the imaging results is evaluated by image entropy, image contrast, and image SNR, as shown in Table 2. The calculation formulas of image entropy $E(\text{image})$ and contrast $C(\text{image})$ are as follows:

$$\begin{cases} E(\text{image}) = -\sum_{n=1}^{N}\sum_{m=1}^{M} p(n,m)\cdot \ln p(n,m), & p(n,m) = \dfrac{|\text{image}(n,m)|^2}{\sum_{j=1}^{N}\sum_{k=1}^{M}|\text{image}(n,m)|^2} \\ C(\text{image}) = \dfrac{1}{u}\sqrt{\dfrac{1}{NM}\cdot\sum_{n=1}^{N}\sum_{m=1}^{M}(|\text{image}(n,m)|-u)^2}, & u = \dfrac{\sum_{n=1}^{N}\sum_{m=1}^{M}|\text{image}(n,m)|}{NM} \end{cases}, \tag{6}$$

where image is the complex image of the imaging result, $p(n,m)$ is the normalized power of the image, u is the average intensity of the image, and N and M denote the two-dimensional pixel points of the image, respectively.

Comparing Figs. 10(a) and 10(b), it is evident that the image entropy of the imaging result is significantly reduced and the image contrast is greatly improved using the SCA to estimate and compensate for the vibration phase error. These show that the SCA can effectively estimate the vibration phase error of the low SNR signals of the airborne SAL. Comparing the focusing effects of Figs. 10(b) and 10(c), it is evident that the image entropy of the imaging result is further reduced, and the image contrast further improved, indicating that the PGA algorithm can effectively estimate the residual phase error after SCA compensation.

4 Imaging Results of Flight Experiment Data

4.1 Time–Frequency Analysis Results and Parameters of the Echo Signal

It should be noted that we did not deploy high-reflectivity cooperative targets on the ground in the flight experiment area corresponding to the blue line box in Fig. 3. After the echo signal was preprocessed, time–frequency analysis was performed on all range gates of the echo signal, which helped in improving the SNR of the echo signal and detecting the target. The window length of the time–frequency analysis was 2.56 ms, and the overlap length was 1.28 ms. Through the time–frequency analysis results, six echo signals were found in the 1.2 s flight experiment data, which were determined to be noncooperative targets with high reflectivity. The target parameters are shown in Table 3. The time–frequency analysis results of the flight experiment data are shown in Fig. 11.

The above results show that time–frequency analysis can effectively improve the SNR of the echo signal, making it relatively easy to browse and detect the echo signal. The above results also show that, unlike periodic vibrations under the simulation conditions, the actual platform vibration situation is more complex, and the photoelectric ball scans in the elevation direction, which leads to a considerable variation in the Doppler center frequency of different slow-time targets. Because the Doppler central frequency cannot be stably concentrated near the theoretical Doppler central frequency, the SNR cannot be effectively improved through filtering. In order

Table 3 Parameters corresponding to six echo signals.

Order number	Range (m)	Slow-time period (s)	Doppler center frequency (kHz)
1	998.475	1.9947 to 2.0254	−26.95
2	1006.875	2.201 to 2.219	31.64
3	1013.663	2.5826 to 2.6036	10.16
4	1015.913	2.6798 to 2.7042	33.985
5	1023.713	2.782 to 2.800	−46.875
6	1026.675	3.0357 to 3.0523	38.54

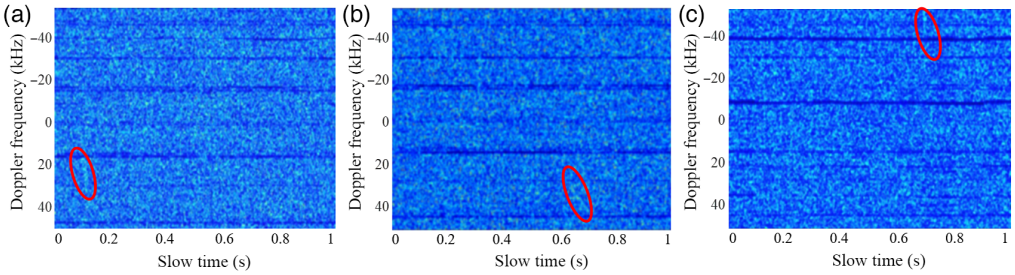

Fig. 11 Time–frequency analysis results of (a) the second echo signal, (b) the fourth echo signal, and (c) the fifth echo signal.

to realize continuous strip imaging, it is necessary to implement vibration phase-error compensation and frequency-shift processing for the echo signal.

4.2 Imaging Results

Subaperture division, dechirping, and frequency shifting were performed on the six echo signals mentioned above. The bandwidth of the Doppler frequency after dechirping the six echo signals was 6 kHz. A narrow-band filter with a bandwidth of 8 kHz was then applied to the echo signals, the SCA was used to estimate and compensate for the vibration phase error, and the PGA algorithm was used to further improve focusing.

Using the third echo signal as an example, the total duration of the signal was ∼21 ms, which could be divided into six subapertures. Figure 12 shows the time–frequency analysis results of each subaperture before and after SCA compensation and after further focusing processing using the PGA algorithm. Figure 12(a) shows that in the case of a low SNR, each subaperture is defocused and cannot be imaged. Figures 12(b) and 12(c) show that after narrow-band filtering and SCA compensation, the signals in each subaperture are initially focused, and the SNR improves. The residual phase error is then compensated using the PGA algorithm, which further improves the focusing effect.

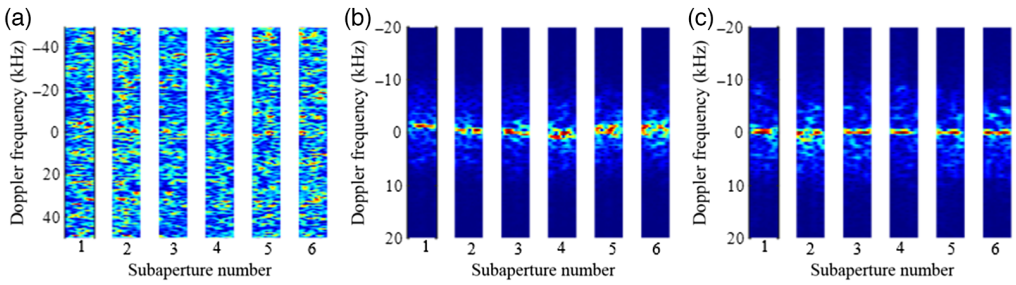

Fig. 12 Time–frequency analysis results of each subaperture: (a) after dechirping, (b) after compensation using the SCA, and (c) after further focusing processing using the PGA algorithm.

According to the POS data corresponding to the period of the above six echo signals, the corresponding Doppler frequency rate was calculated, and a matched filter was constructed. The bandwidth of the matched filter was set to 5 kHz, and the corresponding highest imaging resolution in azimuth was 1.1 cm. The imaging result after SCA compensation is shown in Fig. 13(a), and the imaging results after PGA processing are shown in Fig. 13(b). The target corresponding to the imaging result should be noncooperative targets with high reflectivity (the reflectivity is between the cooperative target and the natural ground object). Evidently, the resolution and SNR were further improved after PGA processing. Figure 13(c) compares the SAL imaging results and the satellite images of this area. The imaging result has a width of 59 m in the azimuth direction and 28 m in the range direction. The broadening of the width in the range direction is due to the scanning of the photoelectric ball at a slight angle in the elevation direction.

The image entropy, image contrast, and image SNR of the imaging results are shown in Table 4. Comparing Figs. 13(a) and 13(b), it is evident that after SCA compensation, the PGA algorithm can be used to compensate for the residual phase error, the image entropy of the imaging result is significantly reduced, the image contrast is greatly improved, and the peak SNR increases to 16 dB. The results show that the method proposed in this paper is essential for phase-error estimations of airborne SAL signals under low SNR conditions.

The imaging result corresponding to the third echo signal in Fig. 13 is shown in Fig. 14. It is evident that there are four scattering points. The azimuth resolution of the imaging result is 1.4 cm, which is close to the theoretical resolution, and three scattering points (with azimuth

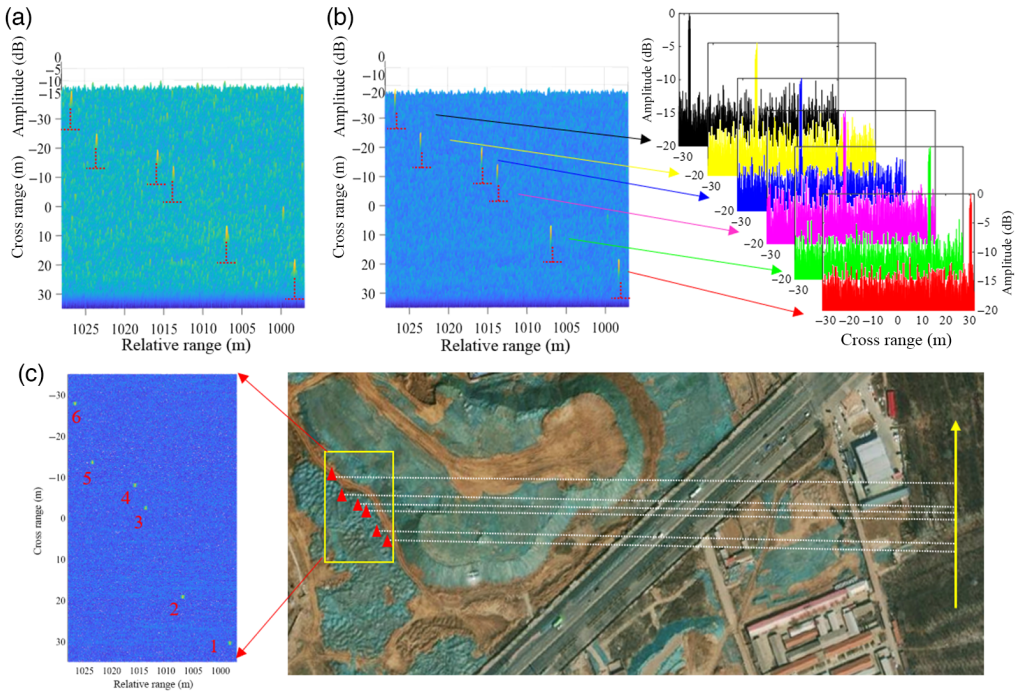

Fig. 13 Imaging results: (a) after compensation using the SCA, (b) after further focusing processing using the PGA algorithm, and (c) comparison between the SAL imaging results and the satellite images.

Table 4 Image entropy, image contrast, and image SNR of imaging results.

	Fig. 13(a)	Fig. 13(b)
Entropy	12.3463	12.0054
Contrast	0.5478	0.6802
SNR (dB)	12	16

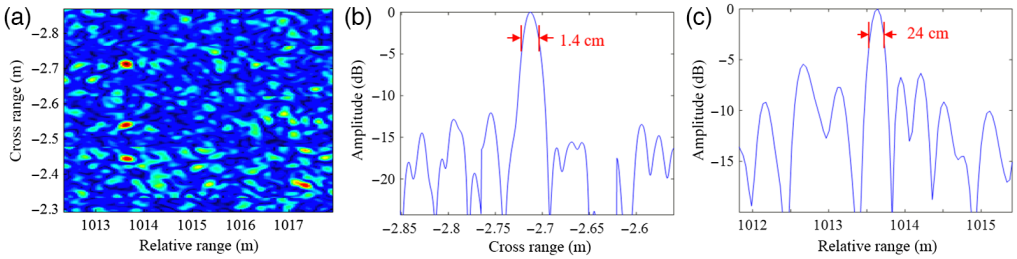

Fig. 14 Imaging result corresponding to the third signal: (a) imaging result, (b) profile in the azimuth direction, and (c) profile in the range direction.

direction spacings of 18.7 and 8.9 cm) on the left-hand side of Fig. 14(a) can be distinguished. The range resolution of the imaging result is 30 cm, and the four scattering points on the left- and right-hand sides (with a range direction spacing of 3.69 m) of Fig. 14(a) can be distinguished.

5 Conclusions

This paper introduces a low SNR signal imaging method when airborne SAL observes noncooperative targets and discusses the imaging results of simulations and experimental data.

This paper used the characteristics of SAL to perform short-time high-resolution imaging and realize long-time strip imaging through subaperture image stitching by subaperture division, parameter estimation of the echo signals, and phase-error compensation. The processing results of the airborne SAL experimental data verified the effectiveness of the proposed method.

Considering that the estimation accuracy of the phase error was limited in the case of a low SNR, in the future design of airborne SAL systems, we should try to improve the single-pulse SNR. Moreover, if the aperture is no longer increased, the peak-power of the laser must first be increased to ensure the imaging and detection performance of noncooperative targets. Additionally, a stabilization platform with better performance should be used.

Code, Data, and Materials Availability

Data underlying the results presented in this paper are not publicly available at this time but may be obtained from the authors upon reasonable request.

Acknowledgments

This work was supported by the National Natural Science Foundation of China (Grant No. 62371440) and the key deployment projects of Chinese Academy of Sciences (Grant No. E03701010F). The authors declare no conflicts of interest.

References

1. B. W. Krause et al., "Synthetic aperture ladar flight demonstration," in *CLEO: 2011 - Laser Sci. to Photonic Appl.*, Baltimore, MD, USA, pp. 1–2 (2011).
2. G. Y. Li et al., "Attitude-error compensation for airborne down-looking synthetic-aperture imaging lidar," *Opt. Commun.* **402**, 355–361 (2017).
3. G. Li et al., "Imaging method for airborne SAL data," *Electron. Lett.* **53**(5), 351–353 (2017).
4. P. Gatt et al., "Performance bounds of the phase gradient autofocus algorithm for synthetic aperture ladar," *Proc. SPIE* **7323**, 73230P (2009).
5. X. X. Zhu et al., "Inverse synthetic aperture radar autofocus imaging of block structure targets with sparse aperture," *J. Appl. Remote Sens.* **17**(1), 016512 (2023).
6. J. H. Gao et al., "Analysis of receiving beam-broaden and detection range of LiDAR based on diffractive optical system," *Chin. J. Lasers* **50**(7), 0510001 (2023).
7. A. J. Cui et al., "Moving target imaging of a dual channel ISAL with binary phase shift keying signals and large squint angles," *Appl. Opt.* **61**(18), 5466–5473 (2022).
8. K. Zhou et al., "Vibration phases estimation based on orthogonal interferometry of inner view field for ISAL imaging and detection," *Appl. Opt.* **62**(11), 2845–2854 (2023).
9. X. Hu et al., "Vibration phases estimation based on multi-channel interferometry for ISAL," *Appl. Opt.* **57**(22), 6481–6490 (2018).

10. X. Hu et al., "Image processing for GEO object with 3D rotation based on ground-based InISAL with orthogonal baselines," *Appl. Opt.* **58**(15), 3974–3985 (2019).
11. D. J. Li et al., "Multi-channel inverse synthetic aperture ladar imaging detection technology and experimental research," *Laser Opt. Prog.* **58**(18), 333–344 (2021).
12. J. H. Gao et al., "Maintenance method of signal coherence in LiDAR and experimental validation," *Opt. Lett.* **47**, 5356–5359 (2022).
13. E. H. Attia et al., "Self-phasing optical heterodyne arrays using the weighted least squares spatial correlation algorithm," *Proc. SPIE* **2120**, 166–177 (1994).

Biographies of the authors are not available.